CrossMark

Anisotropic Size-Dependent Plasticity in Face-Centered Cubic Micropillars Under Torsion

ILL RYU,[1,4] WEI CAI,[2] WILLIAM D. NIX,[3] and HUAJIAN GAO[1]

1.—*Present address:* School of Engineering, Brown University, 182 Hope Street Barus & Holley Bldg., Rm. 737, Providence, RI 02912, USA. 2.—Department of Mechanical Engineering, Stanford University, Stanford, CA 94305-4040, USA. 3.—Department of Materials Science and Engineering, Stanford University, Stanford, CA 94305-4040, USA. 4.—e-mail: ill_ryu@brown.edu

Three-dimensional dislocation dynamics (DD) simulations are performed to investigate the size-dependent plasticity in submicron face-centered cubic (FCC) micropillars under torsion. By using a previously implemented surface nucleation algorithm within DD, we show that the plastic behavior of FCC micropillars under torsion is strongly affected by the crystallographic orientation: In $\langle 110 \rangle$ oriented submicron pillars, coaxial dislocations nucleate and pile up near the axis, leading to homogeneous deformation along the pillars. In contrast, in $\langle 100 \rangle$ and $\langle 111 \rangle$ oriented pillars, heterogeneous plasticity has been observed due to the formation of localized dislocation arrays. As a result of the existence of a coaxial slip plane in $\langle 110 \rangle$ oriented pillars, stronger size-dependent plasticity is observed in this case compared with those in other orientations.

INTRODUCTION

The size-dependent mechanical properties of metals at small scales have been of great interest as the feature dimensions of modern devices are continuously getting smaller. Compared with their bulk counterparts, micron- and submicron-scale metallic samples have shown elevated flow stress in various loading conditions, including micropillar compression/tension,[1–10] wire torsion,[11–14] foil bending,[15–17] and micro- and nano-indentation.[18–20] However, conventional plasticity theories are inherently size independent and unable to capture the observed size effect. In addition, it can be difficult to set up experiments to measure small-scale mechanical responses of materials and to investigate the detailed microstructure during deformation. Recently developed experimental techniques based on in situ transmission electron microscope (TEM)[21–23] and *Laue* micro diffraction[24,25] could provide a large amount of unprecedented information, but it remains challenging to employ these techniques to track evolving dislocation structures in microscale samples.

When materials deform under inhomogeneous loading, the observed size effects are generally attributed to plastic strain gradients associated with geometrically necessary dislocations (GNDs).[26,27] According to strain gradient plasticity (SGP) theories, GNDs are accumulated to accommodate plastic strain gradients, and this leads to additional hardening through GND interaction with statistically stored dislocations (SSDs). However, the SGP theories are usually formulated in a phenomenological way without accounting for the detailed dislocation microstructure.

In this article, we perform dislocation dynamics (DD) simulations to investigate the plastic response of single crystalline metallic submicron pillars under torsion by taking into account the collective behavior of dislocations.[28–37] Our study builds on existing research on the mechanical response of single crystalline metallic micropillars under uniaxial loading. Due to the high surface-to-volume ratio at a small scale, it is necessary to account for dislocation sources not only from dislocation interactions in the interior of the samples but also from nucleation at free surfaces. Most existing DD models consider only the internal sources while ignoring those associated with dislocation nucleation at the surface. To avoid this deficiency, we have previously developed an algorithm within the DD framework to account for dislocation nucleation at free surfaces based on both atomistic modeling and reaction rate

theory.[38] From our DD simulation results, it has been observed that the plastic response of micropillars under torsion is strongly influenced by their crystallographic orientation: In $\langle 110 \rangle$ oriented submicron pillars, Eshelby-like coaxial dislocations nucleate at the surface and pile up near the pillar axis, whereas twist boundaries are formed by array of dislocations in $\langle 100 \rangle$ and $\langle 111 \rangle$ oriented pillars. As a result, homogeneous plastic deformation is observed along the $\langle 110 \rangle$ pillars, while localized plasticity is seen in other orientations. In addition, a stronger size dependence is observed for plasticity in $\langle 110 \rangle$ oriented pillars compared with those in other orientations. The dislocation microstructures from our DD models show qualitative agreement with previous molecular dynamics (MD) simulation of nanowires under torsion.[39,40]

SIMULATION METHODS

A three-dimensional DD model is used to study the size effects of plasticity in FCC submicron pillars. To explore the orientation dependence, we consider micropillars with axes in three high symmetry directions, $\langle 100 \rangle$, $\langle 110 \rangle$, $\langle 111 \rangle$, and diameters ranging from 150 nm to 1000 nm. Isotropic elastic properties are assumed for all orientations for simplicity. The initial dislocation density was chosen to be about 10^{13} m^{-2}. In our DD models, dislocations are represented as a collection of straight segments connected by nodes. The Peach-Koehler force on each dislocation segment is used to update its position through a linear mobility law (for dislocation motion in the viscous drag regime) subject to the glide constraint. Finally, the evolution of dislocation microstructures is obtained by considering topological changes and remesh requirements. The initial dislocation structures consist of randomly distributed dislocation glide loops with junctions naturally formed through a relaxation process described by Motz et al.[33] The height (h)-to-diameter (D) aspect ratio of the pillar is fixed at 5, and the material properties and controlling parameters are summarized in Table I. Periodic boundary conditions are imposed along the axial direction of the pillar. The torque-controlled torsion is applied along

the cylinder axis, and detailed torsion loading mechanism will be described in a later section. For more detailed explanation, the reader is referred to some of the previous publications.[28,38] To obtain reasonable statistics, five simulations are performed for each sample.

Dislocation Nucleation at the Free Surface

At the submicron scales of interest here, plasticity is generally controlled by surface nucleation of dislocations, single-arm operation, and pinning points by voids or impurities. Since mechanical properties at a small scale can be highly sensitive to individual dislocations, it is necessary to take all possible source mechanisms into account in the model. Given ample internal sources from dislocation interactions inside the sample, little attention has been paid, so far, to dislocation sources at the surface. To this end, we have recently developed a simple surface nucleation algorithm within the DD framework.[38] To accommodate surface nucleation, the dislocation nucleation rate (v) is adopted from reaction rate theories based on atomistic models for Cu nanorods,[41,42] as follows:

$$v = v_0 \exp\left(-\frac{Q(\sigma, T)}{k_B T}\right) \qquad (1)$$

where v_0 is the attempt frequency, $k_B T$ the thermal energy, and Q the activation free energy depending on both stress and temperature. Note that σ is the externally applied stress and the internal stress fields of the existing dislocations are neglected in this simple nucleation model. In this study, we focus on plastic flow at room temperature. At a given nucleation rate, the nucleation site is selected following the kinetic Monte Carlo algorithm among randomly distributed N possible nucleation sites on the surface with different stress concentration factors, mimicking surface roughness. Nucleation is allowed to occur by creating a dislocation half loop whose slip system has the maximum resolved shear stress among all $\frac{1}{2}\langle 110 \rangle / \{111\}$ type slip systems. As mentioned,[38] although this simple surface nucleation scheme could provide valuable insights into the governing mechanisms for plastic deformation under uniaxial loading, its direct application to torsion is questionable due to the highly localized character of surface nucleation (because the nucleation model does not account for the internal stress of existing dislocations); dislocation nucleation under uniaxial loading occurs at only a few preferential sites with highest stress concentration factors. In uniaxial loading, nucleated dislocations easily move out of the opposite side of samples without interaction with others, and the plastic flow behavior is not significantly influenced by the localization of nucleation. However, since dislocation pile-ups under torsion and bending have been observed in other DD work and experiments,[17,43,44]

Table I. Material properties (*Cu*) and operating parameters

Material and parameters	Dimension	Value
Shear modulus	[GPa]	48
Poisson ratio	+	0.34
Edge mobility	[Pa^{-1} s^{-1}]	10^5
Screw mobility	[Pa^{-1} s^{-1}]	10^5
Burgers vector length (b)	[m]	2.556×10^{-10}
Temperature	[K]	300
Attempt frequency (v_0)	[sec^{-1}]	1×10^{13}
Coefficient (γ)	+	0.2

the highly localized nucleation could give rise to overestimation of strain hardening from excessive dislocation pile-up.

To overcome this deficiency, we modified the nucleation algorithm to delocalize nucleation sites. Following the mechanistic model to explain the length-induced ductile–brittle transition by Wu et al.,[45] we adjust the stress concentration factor under torsion with respect to a nucleation event as follows:

$$\frac{K_{\text{new}}}{K_{\text{old}}} = \left(1 - \gamma \frac{\Delta\theta_P^{\text{Nuc}}}{\theta_E}\right)\left(\frac{\pi R^2}{\pi R^2 - dS}\right) \qquad (2)$$

where $K_{\text{old}}, K_{\text{new}}$ are the stress concentration factors for the selected nucleation site before and after the nucleation; $\Delta\theta_P^{\text{Nuc}}$ and θ_E are the incremental plastic twist angle per length from the nucleation and elastic twist angle per length, respectively; R is the radius of the micropillar and dS is the projected area change due to the surface step from nucleation; and γ is a constant that describes how nucleation effectively decreases the total torque. The first parenthesis results from a decrease in torsional stress induced by the dislocation nucleation, and the second one describes the stress increase from the cross-sectional area change. In this work, we focus on torsional loading only, whereas delocalized nucleation under tension could be treated in a similar way, as follows:

$$\frac{K_{\text{new}}}{K_{\text{old}}} = \left(1 - \gamma \frac{E\Delta\varepsilon_P^{\text{Nuc}}}{\sigma^{\text{applied}}}\right)\left(\frac{\pi R^2}{\pi R^2 - dS}\right) \qquad (3)$$

where $\Delta\varepsilon_P^{\text{Nuc}}$ is the incremental plastic strain from the nucleation, σ^{applied} is the externally applied stress, and E is Young's modulus. We choose $\gamma = 0.2$, which is found to induce delocalized nucleation under torsion and, at the same time, and not to introduce an artificial hardening under uniaxial loading by lowering the stress concentration factor.

Loading Mechanism for Twist

To apply torsional loading, a constant torque increment is applied until the rate of surface plastic strain overcomes the given tolerance of $5 \times 10^4 \text{ s}^{-1}$, which is chosen to distinguish real strain burst from noise.[38,46] The incremental torque is set to raise the following normalized torque ($\bar{T}$) by an amount equal to 0.05 MPa for all sized samples:

$$\bar{T} = \frac{T}{D^3} = \frac{\mu I_P \theta_E}{8R^3} = \mu \frac{\pi}{16} \frac{R}{L} \varphi_E = \mu \frac{\pi}{16} A \varphi_E \qquad (4)$$

where φ_E is the elastic end-to-end twist angle and I_P is the polar moment of inertia of the cylindrical pillar; D and L are the diameter and length of the cylinder, respectively; μ is the shear modulus; and $A \equiv R/L$ is the aspect ratio. The incremental torque is thus applied by imposing the same increment in twist angle for all sized samples. The length of the

cylinder is fixed by imposing an elastic strain that cancels the plastic strain induced by the dislocations. Under these load conditions, the obtained stress–strain responses are reasonably insensitive to the loading rate under torsion.

To obtain the normalized torque-surface strain curve during torsion, it is necessary to compute the plastic twist due to dislocation motion at each time step. Following Eshelby's analysis of a screw dislocation in a cylinder,[47] we can derive the following expression for the incremental plastic twist per unit length ($\Delta\alpha_P$) by dislocation motion in a cylinder:

$$\Delta\alpha_P = \frac{1}{L \cdot I_p} \sum_k r^k \left(b_z^k n_\theta^k + b_\theta^k n_z^k\right)\Delta A_{\text{swept}}^k \qquad (5)$$

where b^k, n^k, and $\Delta A_{\text{swept}}^k$ are a Burgers vector, slip plane, and swept area of the kth dislocation segment, respectively; and r^k is the distance from the pillar axis to the kth dislocation segment. The detailed derivation will be published elsewhere.[48]

SIMULATION RESULTS

The normalized torques for $\langle 110 \rangle$ oriented micropillars are plotted against the surface total strains and surface plastic strains in Fig. 1a and b with the results clearly showing strong size-dependent plastic flow. As the sample diameter decreases from 1 μm to 150 nm, the normalized torque (which is proportional to the shear stress at the surface) is roughly 50 MPa to 200 MPa at the surface plastic strain of 0.2%. In smaller micropillars, plastic deformation starts at higher stress and exhibits more pronounced strain burst or serrated plastic flow than that in larger pillars, whereas in larger samples, gradual strain hardening takes place under increasing applied torqued, as is typically observed in micro-mechanical measurements. Figure 1c shows that the dislocation densities increase approximately linearly with respect to the surface plastic stain in all sized samples. In $\langle 110 \rangle$ orientated micropillars, a slip plane parallel to the cylinder axis exists that has the maximum resolved shear stress under torsion. According to our nucleation scheme in which the slip plane of a nucleated dislocation is chosen to have the maximum resolved shear stress, screw dislocations parallel to the pillar axis could nucleate at the free surface and glide toward and pile up at the center of the pillar where the resolved stress is almost zero. Due to the modified nucleation algorithm described in the previous section, the nucleation sites change on the free surface every few operations. Figure 1d shows the evolution of dislocation microstructure of a 1-μm pillar as it reaches the plateaued state in the normalized torque-surface plastic strain curve. In all figures showing dislocation microstructures, the colors of the segments indicate the Burgers vectors of the various dislocations, among which the red segments indicate dislocation junctions.

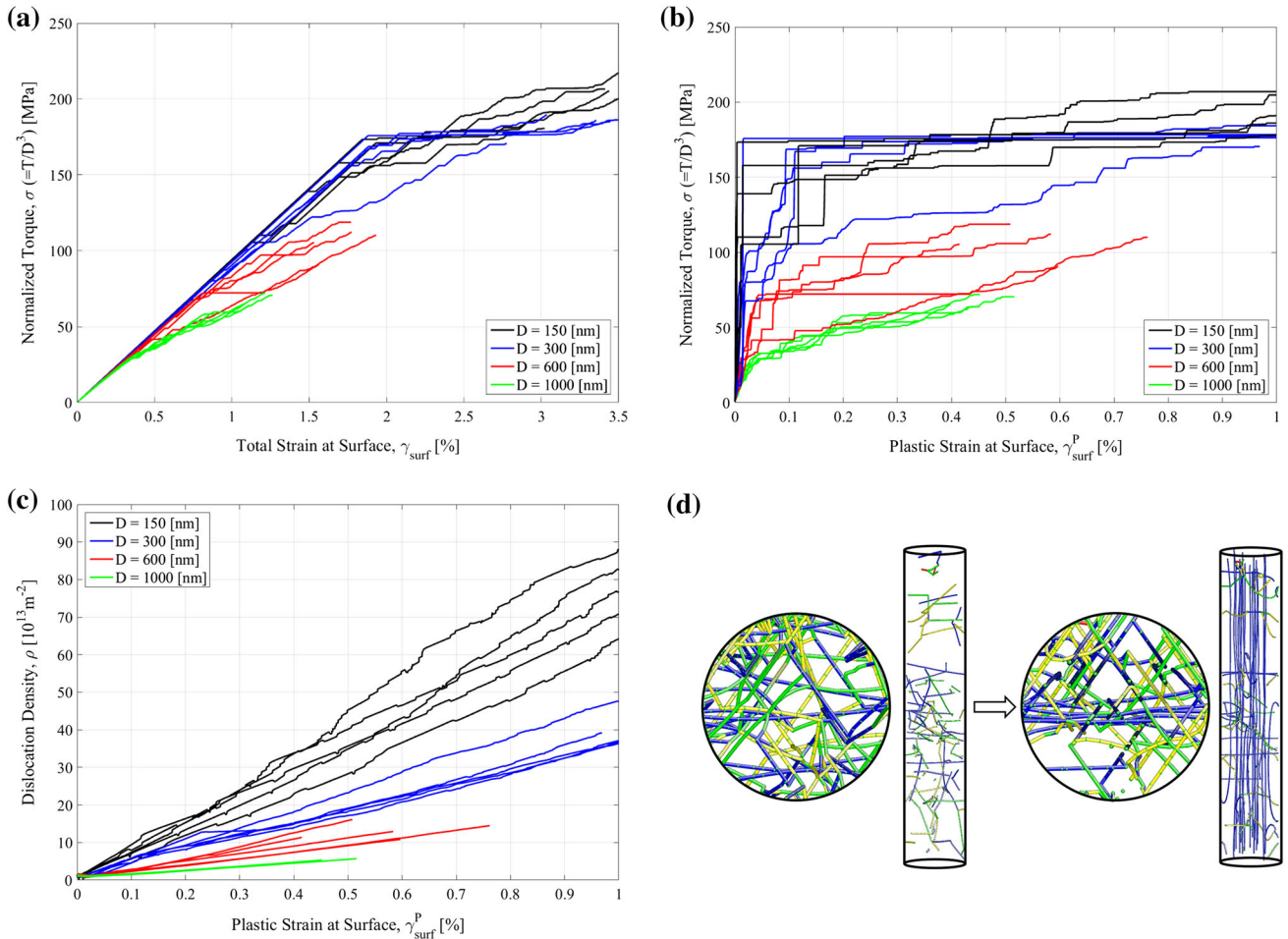**(a)**

(b)

(c)

(d)

Fig. 1. (a) Normalized torque versus total surface strain curves, (b) normalized torque versus plastic surface strain curves, and (c) dislocation density evolution for the 150-nm, 300-nm, 600-nm, and 1000-nm pillars oriented in a $\langle 110 \rangle$ direction under torsion. (d) Dislocation microstructure of a $\langle 110 \rangle$ oriented 1-μm pillar before/after the deformation when viewed along the pillar axis and from the side of the pillar. Microstructure of the deformed pillar is obtained at a plateaued state in the torque-surface plastic strain curve.

For $\langle 111 \rangle$ oriented pillars, the normalized torques are plotted against the surface total strains and surface plastic strains in Fig. 2a and b. Compared with $\langle 110 \rangle$ oriented pillars, the size dependence of plastic flow in $\langle 111 \rangle$ pillars is smaller: The flow stress at 0.2% plastic strain increased from about 150 MPa to 200 MPa as the sample size is reduced from 1 μm to 150 nm. Interestingly, the linear relation between dislocation density and plastic surface strain holds, as shown in Fig. 2c. Although the overall trend of all plots is generally similar to that of $\langle 110 \rangle$ oriented samples, a very different dislocation microstructure has been observed in this orientation. During the initial stage of torsion, preexisting dislocations are reoriented without causing noticeable changes in the normalized torque-surface strain curves. Subsequently, surface nucleation occurs on $\{111\}$ slip planes with the maximum resolved shear stress. Planar dislocation arrays form on the plane perpendicular to the pillar axis, and dislocations are accumulated by the stress

gradient associated with torsion, which is in contrast to the Eshelby-like coaxial dislocation network shown in $\langle 110 \rangle$ oriented micropillars. Figure 2d shows the evolution of a dislocation microstructure of a 1-μm pillar in which, in the deformed configuration, the angle between dislocation arrays in different slip planes are around 60°, which is similar to the formation of hexagonal twist boundaries as shown in MD simulation results in this orientation.[39,40] The fact that hexagonal dislocation arrays do not form on the same slip plane in the DD simulations is caused by the neglect of the internal stress of existing dislocations in the calculation of dislocation nucleation rates.

The corresponding results of $\langle 100 \rangle$ oriented pillars are shown in Fig. 3a and b. In this orientation, the size dependence of plastic flow is smaller than that in $\langle 110 \rangle$ pillars, but it is comparable with that in $\langle 111 \rangle$ pillars: Flow stress is at 0.2% plastic strain, which increases from about 100 MPa to 200 MPa as the sample size is reduced from 1 μm to 150 nm.
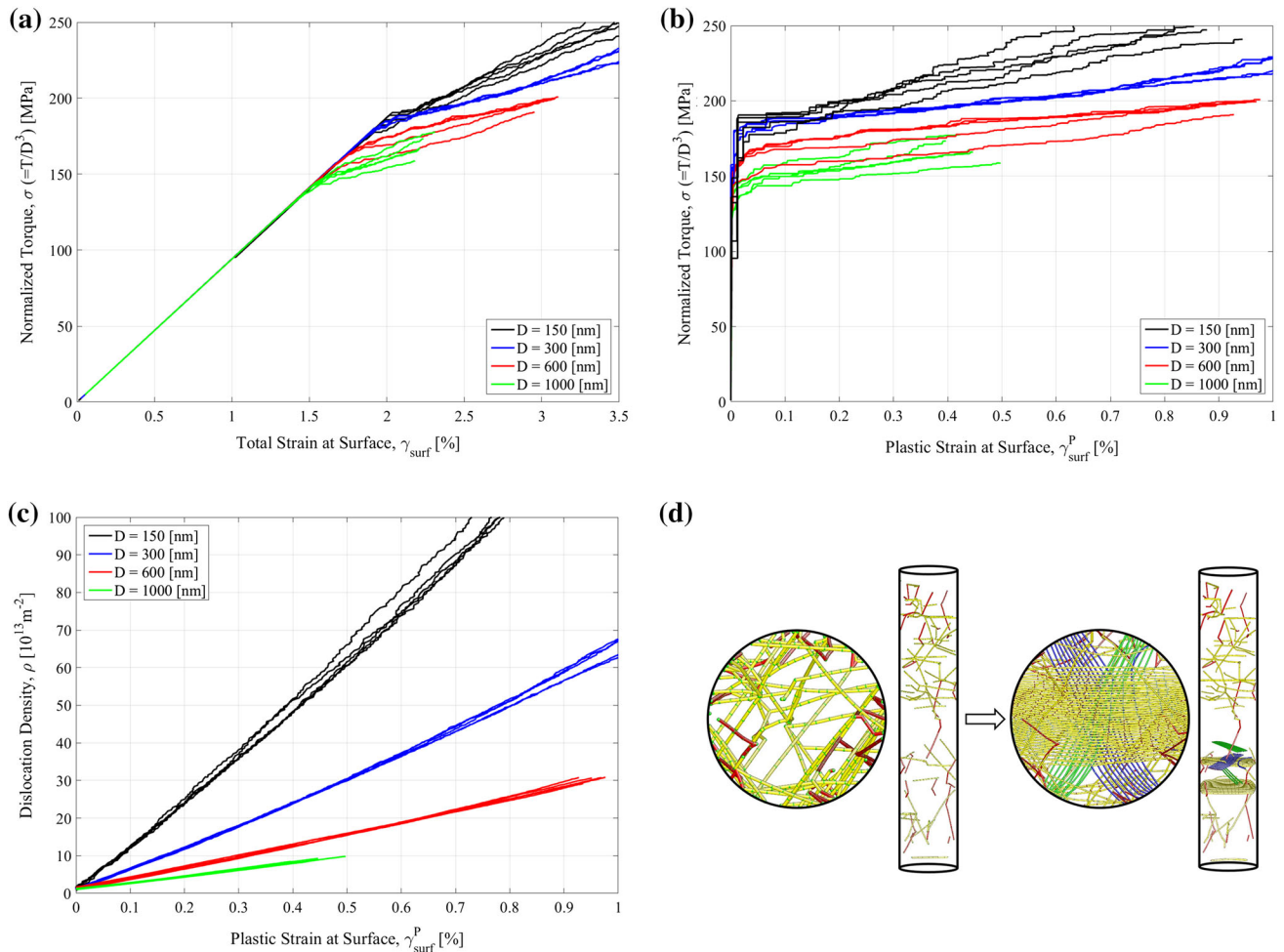
Fig. 2. (a) Normalized torque versus total surface strain curves, (b) normalized torque versus plastic surface strain curves, and (c) dislocation density evolution for the 150-nm, 300-nm, 600-nm, and 1000-nm pillars oriented in a $\langle 111 \rangle$ direction under torsion. (d) Dislocation microstructure of a $\langle 111 \rangle$ oriented 1-μm pillar before/after the deformation.

The dislocation density is again linearly dependent on the plastic surface strain, as shown in Fig. 3c. The plastic flow behaviors and dislocation density evolution in $\langle 100 \rangle$ pillars looks qualitatively similar to those in $\langle 111 \rangle$ pillars. During the initial stage of torsion, the preexisting dislocations rearrange and pile up near the pillar axis, leading to homogeneous plasticity. After surface nucleation occurs at several sites over the free surface, some rectangular (when viewed along the pillar axis) screw dislocation networks start to form, as shown in Fig. 3d.

To see the orientation-dependent size effect of micropillars under torsion more clearly, the normalized torques at 0.3% surface plastic strain are determined and plotted against the corresponding pillar diameters in Fig. 4. The log–log plot shows a strong size dependence in $\langle 110 \rangle$ oriented pillars with an exponent of -0.75, whereas $\langle 100 \rangle$, $\langle 111 \rangle$ orientated samples show a smaller size effect with exponents of -0.22 and -0.17, respectively.

DISCUSSION

For FCC micropillars under uniaxial loading, the size-dependent plasticity is generally believed to be controlled by dislocation sources, depending on the sample size and dislocation density. In micropillars with diameters less than 150 nm, plastic deformation is mainly governed by dislocation nucleation at the surface, whereas for large pillars with diameters close to 1 μm, the operation of truncated sources formed through dislocation interactions is believed to be the governing mechanism. In between these two regimes, both surface nucleation and truncated source operation take place simultaneously.[21,38] However, in torsion, the truncated source operation is effectively hindered by the back stress from dislocation pile-up near the pillar axis and cannot play a major role in plastic deformation. Instead, the GNDs from the strain gradient could facilitate dislocation interaction through the pile-up, which in
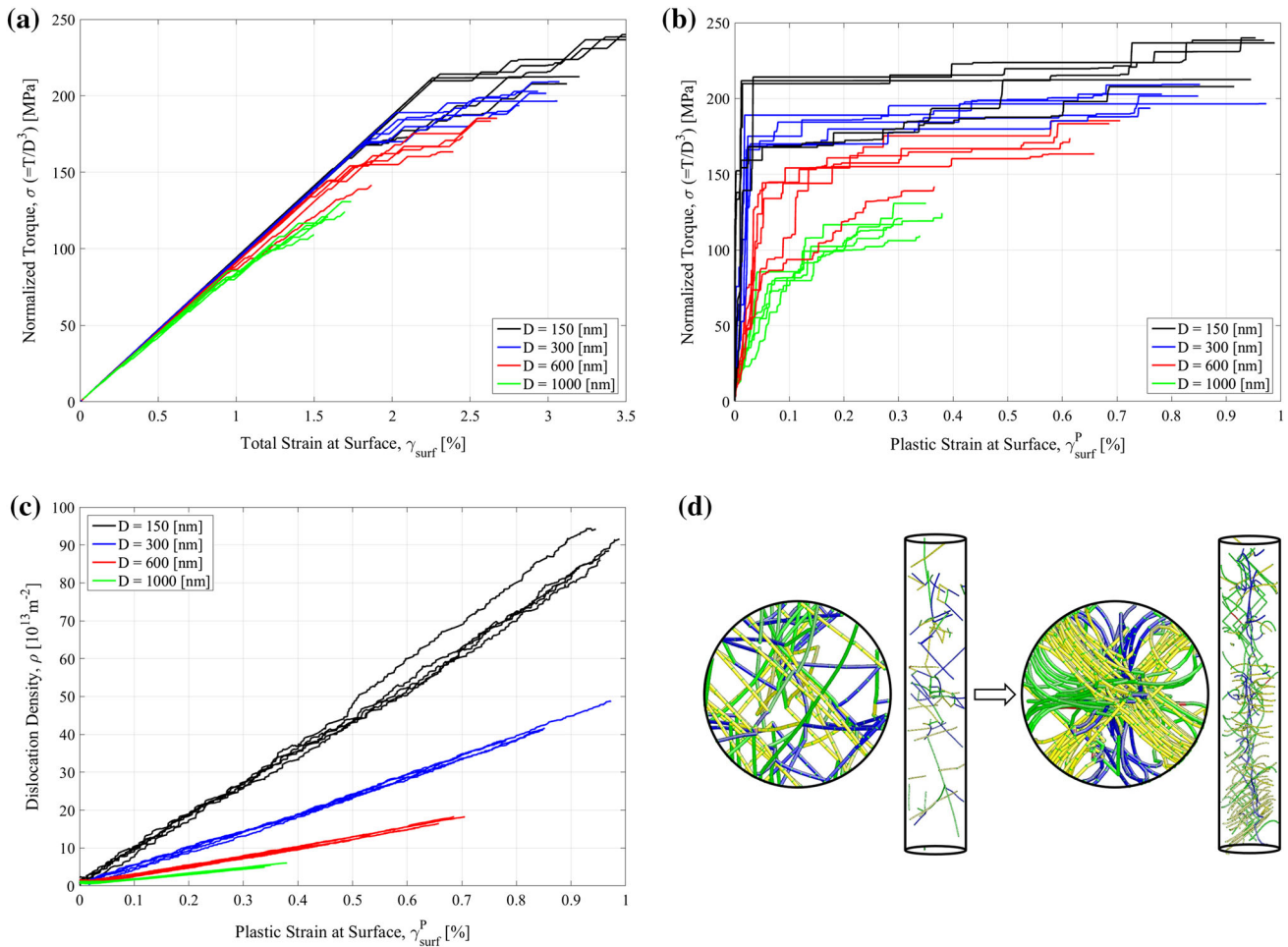
Fig. 3. (a) Normalized torque versus total surface strain curves, (b) normalized torque versus plastic surface strain curves, and (c) dislocation density evolution for the 150-nm, 300-nm, 600-nm, and 1000-nm pillars oriented in a $\langle 100 \rangle$ direction under torsion. (d) Dislocation microstructure of a $\langle 100 \rangle$ oriented 1-μm pillars before/after the deformation.
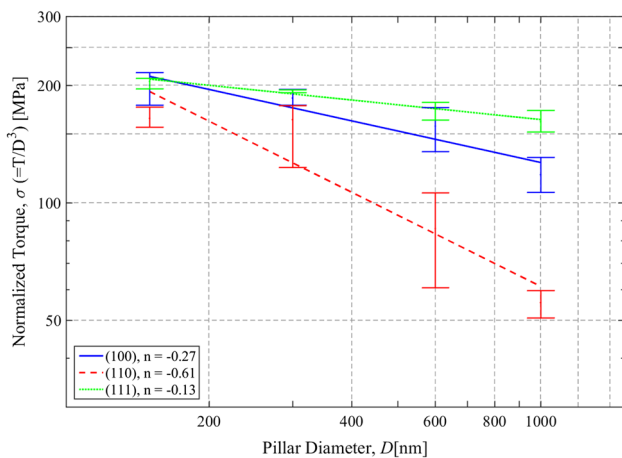

Fig. 4. Size dependence of the normalized torque in $\langle 110 \rangle$, $\langle 111 \rangle$, and $\langle 100 \rangle$ oriented micropillars under torsion. Flow stresses from DD simulations are collected at a surface plastic strain of 0.3%.

turn contributes to an additional size effect. The size effect from the GNDs could be represented by the size exponent in $\langle 100 \rangle$ and $\langle 111 \rangle$ pillars without coaxial dislocations, as shown in Fig. 4. Surprisingly, our DD results show that the size exponent under torsion is actually smaller than that under tension at the same size scale, ranging from 0.5 to 1.0.[21,49,50] This might be understood by the fact that plastic deformation in FCC micropillars is governed by different strengthening mechanisms under uniaxial loading and torsion, namely, single arm operation in tension and dislocation pile-up in torsion, whereas surface nucleation contributes to size effects under both loading conditions.

Our DD simulation results with the modified surface nucleation algorithm show orientation-dependent microstructures during torsion. In $\langle 110 \rangle$ oriented pillars, a coaxial dislocation network is formed after surface nucleation, whereas planar

dislocation arrays are formed in $\langle 111 \rangle$, $\langle 100 \rangle$ pillars. In the latter cases, the angle between dislocation arrays is around 60° for $\langle 110 \rangle$ pillars and 90° for $\langle 100 \rangle$ pillars. These dislocation microstructures are broadly consistent with MD results by Weinberger and Cai.[39,40] However, surface nucleation in our DD models generally occurs at multiple locations and the nucleated dislocations are in parallel with each other, whereas in MD results, dislocation of different Burgers vectors are nucleated on the same plane, leading to the formation of twist boundaries. This discrepancy results from the fact that dislocation nucleation in this simple DD model is not influenced by the stress field of existing dislocations, whereas in MD, that effect is naturally taken into account. However, since the micropillars of interest in this study are significantly larger than the nanowires considered in MD simulations, micropillars may have many nucleation sites on the free surfaces. In addition, the strain rates used in MD models ($\sim 10^8$ s^{-1}) are much higher than those in experiments and in DD. Admittedly, our present nucleation scheme in DD will likely require further improvements to give accurate predictions of the nucleation sites. To understand the nucleation process better, it would also be useful to perform experiments on single crystalline micropillars with in situ electron microscopy.

We could observe stronger size dependence in $\langle 110 \rangle$ oriented micropillars compared with those in other orientations, and the orientation dependence of flow stress is more pronounced in larger pillars, as shown in Fig. 4. It can be attributed to the existence of a slip plane parallel to the pillar axis, on which the pile-ups of coaxial or Eshelby dislocations give rise to a larger amount of plastic deformation due to the larger swept area in this orientation. Especially for the larger pillars, where Taylor hardening can contribute more, the "easy glide" contribution for the $\langle 110 \rangle$ pillars leads to a lower yield stress compared with the $\langle 100 \rangle$ and $\langle 111 \rangle$ pillars.

CONCLUSION

Three-dimensional DD simulations have been performed to investigate the governing mechanisms of size-dependent plasticity in FCC micropillars under torsion. By using a modified surface nucleation scheme, our DD simulations reveal an orientation-dependent size effect in plasticity and provide a detailed dislocation microstructure under torsion. In micropillars oriented along the $\langle 110 \rangle$ direction, plasticity occurs though nucleation of coaxial dislocations, leading to dislocation pile-ups near the pillar axis, while only localized dislocation pile-ups are observed in the inclined slip planes in $\langle 100 \rangle$, $\langle 111 \rangle$ oriented micropillars. Due to the existence of a slip plane for easy glide of coaxial dislocations, a strong size effect is observed in $\langle 110 \rangle$ oriented micropillars. The dislocation microstructure from our DD simulations are in broad agreement with that from MD simulations of much smaller nanowires under torsion.[39,40]

REFERENCES

1. J.R. Greer, W.C. Oliver, and W.D. Nix, *Acta Mater.* 53, 1821 (2005).
2. M.D. Uchic, D.M. Dimiduk, J.N. Florando, and W.D. Nix, *Science* 305, 986 (2004).
3. W.D. Nix, J.R. Greer, G. Feng, and E.T. Lilleodden, *Thin Solid Films* 515, 3152 (2007).
4. J.R. Greer and W.D. Nix, *Phys. Rev. B* 73, 245410 (2004).
5. D. Kiener, W. Grosinger, G. Dehm, and R. Pippan, *Acta Mater.* 56, 580 (2008).
6. K.S. Ng and A.H.W. Ngan, *Acta Mater.* 56, 1712 (2008).
7. D.M. Dimiduk, M.D. Uchic, and T.A. Parthasarathy, *Acta Mater.* 53, 4065 (2005).
8. D.M. Dimiduk, C. Woodward, R. LeSar, and M.D. Uchic, *Science* 312, 1188 (2006).
9. C.A. Volkert and E.T. Lilleodden, *Philos. Mag.* 86, 5567 (2006).
10. D. Kiener, C. Motz, T. Schoberl, M. Jenko, and G. Dehm, *Adv. Eng. Mater.* 8, 1119 (2006).
11. N.A. Fleck, G.M. Muller, M.F. Ashby, and J.W. Hutchinson, *Acta Metall. Mater.* 42, 475 (1994).
12. D.J. Dunstan, B. Ehrler, R. Bossis, S. Joly, K.M.Y. P'ng, and A.J. Bushby, *Phys. Rev. Lett.* 103, 155501 (2009).
13. D.B. Liu, Y.M. He, D.J. Dunstan, B. Zhang, Z.P. Gan, P. Hu, and H.M. Ding, *Int. J. Plasticity* 41, 30 (2013).
14. D.B. Liu, Y.M. He, D.J. Dunstan, B. Zhang, Z.P. Gan, P. Hu, and H.M. Ding, *Phys. Rev. Lett.* 110, 244301 (2013).
15. J.S. Stolken and A.G. Evans, *Acta Mater.* 46, 5109 (1998).
16. M.A. Haque and M.T.A. Saif, *Acta Mater.* 51, 3053 (2003).
17. C. Motz, D. Weygand, J. Senger, and P. Gumbsch, *Acta Mater.* 56, 1942 (2008).
18. Q. Ma and D.R. Clarke, *J. Mater. Res.* 10, 853 (1995).
19. W.D. Nix, *Metall. Trans. A* 20, 2217 (1989).
20. N.A. Stelmashenko, M.G. Walls, L.M. Brown, and Y.V. Milman, *Acta Metall. Mater.* 41, 2855 (1993).
21. D. Kiener and A.M. Minor, *Nano Lett.* 11, 3816 (2011).
22. S.H. Oh, M. Legros, D. Kiener, and G. Dehm, *Nat. Mater.* 8, 95 (2009).
23. Z.W. Shan, R.K. Mishra, S.A.S. Asif, O.L. Warren, and A.M. Minor, *Nat. Mater.* 7, 115 (2008).
24. G. Feng, A.S. Budiman, W.D. Nix, N. Tamura, and J.R. Patel, *J. Appl. Phys.* 104, 043501 (2008).
25. A.S. Budiman, W.D. Nix, N. Tamura, B.C. Valek, K. Gadre, J. Maiz, R. Spolenak, and J.R. Patel, *Appl. Phys. Lett.* 88, 233515 (2006).
26. M.F. Ashby, *Philos. Mag.* 21, 399 (1970).
27. A. Arsenlis and D.M. Parks, *Acta Mater.* 47, 1597 (1999).
28. A. Arsenlis, W. Cai, M. Tang, M. Rhee, T. Oppelstrup, G. Hommes, T.G. Pierce, and V.V. Bulatov, *Model Simul. Mater. Sci.* 15, 553 (2007).
29. B. Devincre and L.P. Kubin, *Mater. Sci. Eng. A* 234, 8 (1997).
30. J.A. El-Awady, M. Wen, and N.M. Ghoniem, *J. Mech. Phys. Solids* 57, 32 (2009).

31. H.D. Espinosa, M. Panico, S. Berbenni, and K.W. Schwarz, *Int. J. Plasticity* 22, 2091 (2006).
32. Z.L. Liu, X.M. Liu, Z. Zhuang, and X.C. You, *Scripta Mater.* 60, 594 (2009).
33. C. Motz, D. Weygand, J. Senger, and P. Gumbsch, *Acta Mater.* 57, 1744 (2009).
34. K.W. Schwarz, *J. Appl. Phys.* 85, 120 (1999).
35. D. Weygand, L.H. Friedman, E. van der Giessen, and A. Needleman, *Mater. Sci. Eng. A* 309, 420 (2001).
36. C.Z. Zhou, S.B. Biner, and R. LeSar, *Acta Mater.* 58, 1565 (2010).
37. R.S. Fertig and S.P. Baker, *Prog. Mater Sci.* 54, 874 (2009).
38. I. Ryu, W. Cai, W.D. Nix, and H. Gao, *Acta Mater.* 95, 176 (2015).
39. C.R. Weinberger and W. Cai, *J. Mech. Phys. Solids* 58, 1011 (2010).
40. C.R. Weinberger and W. Cai, *Nano Lett.* 10, 139 (2010).

41. S. Ryu, K. Kang, and W. Cai, *Proc. Nat. Acad. Sci.* 108, 5174 (2011).
42. S. Ryu, K. Kang, and W. Cai, *J. Mater. Res.* 26, 2335 (2011).
43. J. Senger, D. Weygand, O. Kraft, and P. Gumbsch, *Model Simul. Mater. Sci.* 19, 074004 (2011).
44. C. Motz and D.J. Dunstan, *Acta Mater.* 60, 1603 (2012).
45. Z.X. Wu, Y.W. Zhang, M.H. Jhon, H.J. Gao, and D.J. Srolovitz, *Nano Lett.* 12, 910 (2012).
46. S.W. Lee, A.T. Jennings, and J.R. Greer, *Acta Mater.* 61, 1872 (2013).
47. J.D. Eshelby, *J. Appl. Phys.* 24, 176 (1953).
48. I. Ryu, W. Cai, W.D. Nix, and H. Gao, Unpublished research (2015).
49. A.T. Jennings, M.J. Burek, and J.R. Greer, *Phys. Rev. Lett.* 104, 135503 (2010).
50. D. Kiener and A.M. Minor, *Acta Mater.* 59, 1328 (2011).